

Warm H₂ in the Galactic center region [★]

N.J. Rodríguez-Fernández¹, J. Martín-Pintado¹, A. Fuente¹, P. de Vicente¹, T.L. Wilson^{2,3}, and S. Hüttemeister⁴

¹ Observatorio Astronómico Nacional, IGN, Apartado 1143, E-28800 Alcalá de Henares, Spain; nemesio@oan.es

² Max-Planck-Institut für Radioastronomie, Postfach 2024, D-53010 Bonn, Germany

³ Sub-mm Telescope Observatory, Steward Observatory, The University of Arizona, Tucson, AZ 85728, USA

⁴ Radioastronomisches Institute der Universität Bonn, Auf dem Hügel 71, D-53121 Bonn, Germany

Received; accepted

Abstract. We present ISO observations of several H₂ pure-rotational lines (from S(0) to S(5)) towards a sample of 16 molecular clouds distributed along the central ~ 500 pc of the Galaxy. We also present C¹⁸O and ¹³CO $J = 1 \rightarrow 0$ and $J = 2 \rightarrow 1$ observations of these sources made with the IRAM-30m telescope. With the CO data we derive H₂ densities of $10^{3.5-4.0}$ cm⁻³ and H₂ column densities of a few 10^{22} cm⁻². We have corrected the H₂ data for ~ 30 magnitudes of visual extinction using a self-consistent method. In every source, we find that the H₂ emission exhibits a large temperature gradient. The S(0) and S(1) lines trace temperatures (T) of ~ 150 K while the S(4) and S(5) lines indicate temperatures of ~ 600 K. The warm H₂ column density is typically $\sim 1 - 2 \times 10^{22}$ cm⁻², and is predominantly gas with $T=150$ K. This is the first direct estimate of the total column density of the warm molecular gas in the Galactic center region. These warm H₂ column densities represent a fraction of $\sim 30\%$ of the gas traced by the CO isotopes emission. The cooling by H₂ in the warm component is comparable to that by CO. Comparing our H₂ and CO data with available ammonia (NH₃) observations from literature one obtains relatively high NH₃ abundances of a few 10^{-7} in both the warm and the cold gas. A single shock or Photo-Dissociation Region (PDR) cannot explain all the observed H₂ lines. Alternatives for the heating mechanisms are discussed.

Key words: ISM: clouds – ISM: molecules – ISM: dust, extinction – Galaxy: center – Infrared: ISM: continuum – Infrared: ISM: lines and bands

1. Introduction

The interstellar matter in the inner few hundreds parsecs of the Galaxy (hereafter GC) is mainly molecular. In this

Send offprint requests to: N.J. Rodríguez-Fernández

[★] Based on observations with ISO, an ESA project with instruments funded by ESA Member States (especially the PI countries: France, Germany, the Netherlands and the United Kingdom) and with the participation of ISAS and NASA.

region there are molecular clouds and huge cloud complexes like Sgr B2 which can be as large as 70 pc, with masses of 10^6 solar masses. The physical conditions in the GC clouds differ appreciably to those of the clouds of the disk of the Galaxy. The GC clouds have average densities of $\sim 10^4$ cm⁻³ instead of 10^2 cm⁻³ typical of the clouds of the disk. In addition, with widespread high temperatures (up to 200 K), GC clouds are hotter than disk clouds.

The temperatures of the warm gas are known mainly by observations of ammonia (NH₃) metastable lines. Güsten et al. (1981, 1985) derived rotational temperatures (T_{rot}) of 60-120 K in several GC clouds, most of them in the Sgr A complex. Morris et al. (1983) showed that $T_{\text{rot}} \sim 30 - 60$ K are common in the region $|l| < 2^\circ$. The most complete study of the temperature structure of the molecular gas in the GC, was carried out by Hüttemeister et al. (1993). They presented a multilevel study of NH₃ metastable lines of 36 molecular clouds distributed all along the “Central Molecular Zone” (CMZ, in notation of Morris & Serabyn 1996) and the “Clump 2” complex, which, although not belonging to the actual CMZ, exhibits similar properties. They detected warm gas at all galactic longitudes and showed that the NH₃ emission can be characterized by two temperature components since the T_{rot} derived from the (1,1) and (2,2) levels is $\sim 20 - 30$ K and that derived from the (4,4) and (5,5) levels is $\sim 70 - 200$ K. Unfortunately, the *a priori* unknown abundance of the NH₃ molecule has made it difficult to estimate the total column density of warm gas in the GC clouds.

The heating of the molecular gas over large regions (~ 10 pc) where the dust temperature is lower than 30 K (Odenwald & Fazio 1984, Cox & Laureijs 1989, Martín-Pintado et al. 1999, Rodríguez-Fernández et al. 2000) is a puzzle. Indirect arguments such as the large widths of molecular lines or large abundances in gas phase of molecules such as SiO (Martín-Pintado et al. 1997, Hüttemeister et al. 1998) or NH₃ points towards a mechanical heating. Wilson et al. (1982) proposed the dissipation

of turbulence induced by differential Galactic rotation as a possible heating source.

For the first time, we have measured the total column densities of warm gas in the GC clouds by observing the lowest H₂ pure-rotational transitions with the *Infrared Space Observatory* (ISO; Kessler et al. 1996). The H₂ pure-rotational lines trace gas with temperatures of a few hundred K (see Shull & Beckwith 1982 for a review on the properties and the notation of the H₂ molecule). ISO has detected H₂ pure-rotational lines in a variety of sources such as: Young Stellar Objects (Van den Ancker 1999); galactic nuclei (see e.g. Kunze et al. 1999); Photo Dissociation Regions (PDRs) like NGC 7023 (Fuente et al. 1999, 2000) or S140 (Timmermann et al. 1996); shock-excited sources such as Orion Peak 1 (Rosenthal et al. 2000); and proposed x-ray excited regions (XDRs) like RCW 103 (see Wright 2000).

Our sample consists of 18 molecular clouds from the samples of Hüttemeister et al. (1993) and Martín-Pintado et al. (1997). Two of these show a non-equilibrium H₂ ortho-to-para ratio and have been studied in detail by Rodríguez-Fernández et al. (2000). In this paper we present the other 16 clouds of the sample. The clouds are distributed along the CMZ, from the Sgr E region to the vicinity of Sgr D and the “Clump 2” complex. Four clouds are located in the Sgr C complex, three in the vicinity of Sgr A (two are in the radio Arc). Two clouds are situated in the cold dust ridge reported by Lis & Carlstrom (1994) that seems to connect the radio Arc and Sgr B. Other three clouds belong to the Sgr B complex.

This paper is organized as follows. In Sect. 2 we present C¹⁸O and ¹³CO IRAM-30m observations and H₂ ISO observations. The analysis of the CO isotopes and H₂, is presented in Sect. 3 and 4, respectively. The results and the possible heating mechanism of the warm gas are discussed in Sect. 5.

2. Observations

2.1. IRAM 30-m observations and results

We have observed the $J = 1 \rightarrow 0$ and $J = 2 \rightarrow 1$ lines of ¹³CO and C¹⁸O with the IRAM 30-m telescope (Pico de Veleta, Spain) towards the GC molecular clouds given in Table 1. This table also gives the pointing positions and the complexes where the clouds belong. Figure 1 shows the position of the sources overlaid on the large scale C¹⁸O($1 \rightarrow 0$) map of Dahmen et al. (1997). The observations were carried out in May 1997, May 1998 and June 2000. The $J = 1 \rightarrow 0$ and $J = 2 \rightarrow 1$ lines were observed simultaneously, with two 512 × 1 MHz channel filter banks connected to two SIS receivers at 3 and 1.3 mm. The receivers were tuned to single side band mode. The image rejection, checked against standard calibration sources, was always larger than 10 dB. Typical system temperatures were ~ 250 K for the $J = 1 \rightarrow 0$ lines and ~ 400 K for

the $J = 2 \rightarrow 1$ lines. The velocity resolution obtained with this configuration was 2.7 and 1.4 km s⁻¹ at 3 and 1.3 mm respectively. The beam size of the telescope was 22'' for the $J = 1 \rightarrow 0$ lines and 11'' for the $J = 2 \rightarrow 1$ line. Pointing and focus were monitored regularly. The pointing corrections were never larger than 3''. The spectra were taken in position switching with a fixed reference position at $(l, b) = (0^\circ 65, 0^\circ 2)$, which was selected from the ¹³CO map of Bally et al. (1987). Calibration of the data was made by observing hot and cold loads with known temperatures, and the line intensities were converted to main beam brightness temperatures, T_{MB} , using main beam efficiencies of 0.68 and 0.41 for 3 and 1.3 mm respectively. The main beam efficiencies for the observations of June 2000 are 0.80 and 0.53 for 3 and 1.3 mm respectively.

A sample of spectra is shown in Fig. 2. Most of the sources show CO emission in several velocity components with Gaussian line profiles. However, in some clouds the different components are blended, giving rise to more complex profiles. The observed parameters derived from Gaussian fits are listed in Table 2.

2.2. ISO observations and results

Several H₂ pure-rotational lines (from S(0) to S(5)) have also been observed towards the molecular clouds given in Table 1. The observations were carried out with the *Short Wavelength Spectrometer* (SWS; de Graauw et al. 1996) on board ISO. The sizes of the SWS apertures at each wavelength are listed in Table 3. The orientation of the apertures on the sky varies from source to source, but it is within position angle 89.34° and 93.58° for all the observations (measuring the angles anti-clockwise between north and the short sides of the apertures).

The observations presented in this paper are the result of two different observing proposals. In one of them only the S(0), S(1) and S(3) lines were observed, in the second one all the lines from the S(0) to the S(5) but the S(2) were observed. The wavelength bands were scanned in the SWS02 mode with a typical on-target time of 100 s. Three sources were also observed in the SWS01 mode but the signal-to-noise ratio of these observations is rather poor and will not be discussed in this paper. Data were processed interactively at the MPE from the Standard Processed Data (SPD) to the Auto Analysis Results (AAR) stage using calibration files of September 1997 and were reprocessed automatically through version 7.0 of the standard Off-Line Processing (OLP) routines to the AAR stage. The two reductions give similar results. In this paper we present the results of the reduction with OLP7.0. The analysis has been made using the ISAP2.0¹ software

¹ The ISO Spectral Analysis Package (ISAP) is a joint development by the LWS and SWS Instrument Teams and Data Centers. Contributing institutes are CESR, IAS, IPAC, MPE, RAL and SRON.

package. With ISAP we have zapped the bad data points and averaged the two scan directions for each of the 12 detectors. Then, we have shifted (flatfielded) the different detectors to a common level using the medium value as reference and finally, we have averaged the 12 detectors and rebinned to one fifth of the instrumental resolution. No defringing was necessary since the continuum flux at these wavelengths ($\lambda < 30\mu\text{m}$) is lower than 30 Jy for all the clouds.

Baseline (order 1) and Gaussian fitting to the lines have also been carried out with ISAP. The spectra are shown in Fig. 3 and the observed fluxes as derived from the fits are listed in Table 3. The absolute flux calibration errors are less than 30, 20, 25, 25, and 15% for the S(0), S(1), S(3), S(4), and S(5) lines, respectively (Salama et al. 1997). Because of the medium spectral resolution of the SWS02 mode ($\lambda/\Delta\lambda \sim 1000 - 2000$) and the wavelength calibration uncertainties ($\sim 15 - 50 \text{ km s}^{-1}$ depending on the wavelength, see Valentijn et al. 1996), it is difficult to undertake a detail comparison between the kinematics of the H₂ lines and those of the ¹³CO and C¹⁸O lines. Table 3 lists the radial velocities of the S(1) lines, which have the higher signal-to-noise ratio. Within the calibration uncertainties, the radial velocity of the H₂ lines agrees with at least one of the ¹³CO components listed in Table 2.

Unfortunately, the lack of resolution does not allow us to establish if the H₂ emission is indeed arising from just one or several of the CO velocity components since, in general, all of them are within the velocity range of the unresolved H₂ emission. M-0.96 + 0.13 is the only cloud for which we can say that the warm H₂ is not likely to arise in all the velocity components seen in CO. The CO components are centered at -110, 11, and 133 km s^{-1} , while the H₂ S(1) line is centered at -70 km s^{-1} . Even with the spectral resolution of the SWS02 mode, one can see that the CO component with *forbidden* velocities (133 km s^{-1}) is not likely to contribute to the H₂ emission.

Table 3 also lists the widths of the H₂ S(1) lines. The H₂ line widths of the GC clouds tend to be larger than the instrumental resolution for extended sources ($\sim 170 \text{ km s}^{-1}$ for the S(1) line, see Lutz et al. 2000). This is due to the large intrinsic line widths typical of the GC clouds and mainly, to the presence of several velocity components along the line of sight that contribute to the H₂ emission. However, not all the sources that show CO emission in several velocity components have line widths larger than $\sim 170 \text{ km s}^{-1}$ (for instance M+0.83 - 0.10 or M+0.16 - 0.10). This implies that not all the CO velocity components detected in these sources are contributing to the H₂ emission, although it is difficult to discriminate which ones are emitting in H₂.

3. C¹⁸O and ¹³CO column densities

The excitation analysis of the three lowest C¹⁸O rotational lines by Hüttemeister et al. (1998) shows that the

CO emission could arise in cold (20-30 K) and dense (10^4 cm^{-3}) gas or warmer ($\gtrsim 100 \text{ K}$) and less dense gas (10^3 cm^{-3}). However, the large column densities of cold ($\sim 25 \text{ K}$) dust (Martín-Pintado et al. 1999; Rodríguez-Fernández et al. 2000) suggest that most of the $J = 1 \rightarrow 0$ and $J = 2 \rightarrow 1$ CO emission should arise from cold and dense gas coupled to the dust.

We have derived physical conditions and gas column densities from the C¹⁸O and ¹³CO data using the Large Velocity Gradient (LVG) approximation (see e.g. Hüttemeister et al. 1998). Assuming a kinetic temperature (T_K) of 20 K, we have constrained the H₂ densities (n_{H_2}) from the $J = 2 \rightarrow 1$ to $J = 1 \rightarrow 0$ C¹⁸O ratio (or the same ratio of ¹³CO for a few sources, see Table 2). Then, we have derived the C¹⁸O and ¹³CO column densities ($N_{\text{C}^{18}\text{O}}$ and $N_{^{13}\text{CO}}$) for corresponding n_{H_2} , using the $J = 1 \rightarrow 0$ lines intensities. The results of the analysis are listed in Table 2. Typical C¹⁸O $J = 2 \rightarrow 1$ to $J = 1 \rightarrow 0$ line ratios are $\sim 1.0 - 1.5$ which give n_{H_2} of $\sim 10^{3.5-4.0} \text{ cm}^{-3}$ for $T_K=20 \text{ K}$. The typical integrated intensities of the C¹⁸O ($J = 1 \rightarrow 0$) lines ($\sim 3 - 9 \text{ K km s}^{-1}$) imply $N_{\text{C}^{18}\text{O}}$ of $\sim 2 - 8 \cdot 10^{15} \text{ cm}^{-2}$. $N_{^{13}\text{CO}}$ is approximately a factor of 10 larger than $N_{\text{C}^{18}\text{O}}$. Since the expected abundance ratio of the two species in the GC is 12.5 (Wilson & Matteucci 1992), the observed ratio indicates that both lines are optically thin. We can also explain the observed CO lines ratios and intensities with higher kinetic temperatures (see above). For instance, for $T_K=100 \text{ K}$ one would obtain H₂ densities which are lower by a factor of ~ 2.5 . However, even in the unrealistic case that all the $J = 1 \rightarrow 0$ and $J = 2 \rightarrow 1$ CO arise in warm gas with $T_K=100 \text{ K}$, the column densities do not change more than 10% with respect to those at low temperature. Thus, in general, if one considers a mixture of warm and cool gas the total column densities traced by CO will be similar to those derived with $T_K=20 \text{ K}$.

Table 2 also gives the estimated H₂ column densities as derived from $N_{^{13}\text{CO}}$ assuming that the abundance of ¹³CO relative to H₂ is $5 \cdot 10^{-6}$. This ratio is based on the ¹³C/¹²C isotopic ratio in the Galactic center of 1/20 (Wilson & Matteucci 1992) and a CO/H₂ ratio of 10^{-4} (see e.g. Hüttemeister et al. 1998 and references therein). The typical H₂ column densities derived for the main velocity components in all the sources are of a few 10^{22} cm^{-2} .

4. Warm H₂

Table 3 lists the observed fluxes of the H₂ lines. The most intense lines are the S(0) ($J = 2 \rightarrow 0$) and S(1) ($J = 3 \rightarrow 1$) lines, with typical fluxes of $0.5 - 1 \cdot 10^{-19}$ and $1 - 2 \cdot 10^{-19} \text{ W cm}^{-2}$, respectively. Unfortunately, the S(2) line was only observed in the two clouds already discussed in detail by Rodríguez-Fernández et al. (2000). The S(3) line is very weak and it has only been detected in the sources with more intense S(1) emission. Even in some sources which show emission in the S(4) and S(5) lines, the S(3) line has not been detected. This is due to strong

dust absorption produced by the solid state band of the silicates at 9.7 μm (Martín-Pintado et al. 1999).

The pure rotational lines of H₂ arise due to electric quadrupole transitions. The quadrupole transition probabilities are small (Turner et al. 1977) and thus the rotational lines remain optically thin. In this case, the column density of the upper level involved in a transition from level i to level j can be obtained from the line fluxes F_{ij} of Table 3 using the following expression:

$$N_i = \frac{\lambda_{ij}}{hc} \frac{4\pi F_{ij} e^{\tau_{ij}}}{\Omega_{ij} A_{ij}}$$

where λ_{ij} and A_{ij} are the wavelength and the quadrupole probability of the transition, and τ_{ij} and Ω_{ij} are the dust opacity and the aperture at λ_{ij} , respectively. Since the column densities are averaged on the ISO apertures, in the case of extended sources (assumed homogeneous), it is not necessary to apply any additional correction to account for the different ISO apertures (see also Rodríguez-Fernández et al. 2000).

4.1. Extinction and ortho-to-para ratio

Figure 4 shows the population diagrams for one of the sources for which more than four lines were detected: M-0.32 - 0.19. It shows, for each observed line, the logarithm of the upper level population divided by both the rotational and nuclear spin degeneracy, i.e. $3(2J + 1)$ for the ortho levels (odd J) and $(2J + 1)$ for the para levels (even J).

The filled circles show the populations without any extinction correction. One can see that the population in the $J=5$ level is lower than expected from the interpolation from the other levels. As discussed in Rodríguez-Fernández et al. (2000), this fact can be used to estimate the total extinction caused by the dust located between the observer and the H₂ emitting region. Once an extinction law is assumed, we can correct the H₂ line intensities by increasing the visual extinction until the column density in any level (in particular that in the $J=5$ level) is consistent with the column densities derived for the other levels, i.e. until the population diagrams are smooth curves.

We have used the extinction law derived by Lutz (1999) towards the Galactic center using Hydrogen recombination lines. This extinction law differs from that of Draine (1989) for silicate-graphite mixtures of grains in that there is no deep minimum at $\sim 7 \mu\text{m}$ and there is a slightly higher value for the $A_{9.7\mu\text{m}}/A_V$ ratio, where A_V the visual extinction (at 0.55 μm) and $A_{9.7\mu\text{m}}$ is the extinction at 9.7 μm . For instance, in the case of M-0.32 - 0.19 one sees that 15 mag of visual extinction (squares in Fig. 4) is a lower limit to the extinction while 45 mag (stars in Fig. 4) is an upper limit. The best result is obtained for a visual extinction of around 30 mag (triangles). Using this method for the other sources with more than four lines detected, we also derive a visual extinction of ~ 30 . This value should be considered as a lower limit to the actual

extinction for the sources where the S(3) line was not detected. It is not possible to know how much of this extinction is caused by material in the line-of-sight towards the GC (*foreground extinction*) and how much is intrinsic to the GC clouds. Nevertheless, a visual extinction of ~ 30 mag is in agreement with the average *foreground extinction* as measured by Catchpole et al. (1990) using stars counts and suggests that the H₂ emission can arise from the clouds surfaces (see also Pak, Jaffe & Keller 1996). In the other sources where we cannot estimate the extinction from our H₂ data we have applied a correction of $A_V=30$ mag. For those clouds located farther from the center of the Galaxy and/or the Galactic plane, we have corrected the observed fluxes by 15 mag (see Table 4). This value was derived by Rodríguez-Fernández et al. (2000) by analyzing the far infrared dust emission toward two sources in the ‘‘Clump 2’’ and the $l=1.5^\circ$ complexes. In any case, the extinction correction has a minor impact in the main results of this paper (see below). Figure 5 shows the extinction corrected population diagrams for all the sources presented in this paper.

The values of extinction required to give a smooth population diagram would be somewhat smaller if the H₂ ortho-to-para (OTP) ratio were lower than the local thermodynamic equilibrium (LTE) ratio. This is obvious since the method to derive the extinction depends mainly on the extinction at the wavelength of an ortho level ($J=5$). Non-equilibrium OTP ratios measured with the lowest rotational lines has been found in two clouds of our sample (Rodríguez-Fernández et al. 2000). Unfortunately, for the clouds presented in this paper, it is difficult to estimate the OTP ratio since the S(2) line has not been observed and the S(3) line is completely extinguished in most of them. Current data do not show any evidence for a non-equilibrium OTP ratio, but we cannot rule it out *a priori*. For instance, assuming OTP ratios of ~ 2 we still can find a smooth population diagrams, i.e. without the typical zig-zag shape characteristic of non-equilibrium OTP ratios (see. e.g. Fuente et al. 1999). In this case, the extinction would be of $\sim 20 - 25$ mag instead of 30 mag. On the contrary, assuming OTP ratios of ~ 1 one finds, in general, rather artificial diagrams, which suggests that OTP ratios as low as ~ 1 are not compatible with the data. Although one must bear in mind these considerations, in the following we assume that the OTP ratios are LTE.

4.2. H₂ column densities and excitation temperatures

Table 4 lists the results derived from the H₂ lines after applying the extinction corrections. The excitation temperature derived from the $J=3$ and $J=2$ levels (T_{32}) is between 130 and 200 K while the excitation temperature derived from the $J=7$ and $J=6$ levels (T_{76}) is $\sim 500 - 700$ K. The temperatures are only 15-20 % larger than those one obtains without any extinction correction. For the four clouds in which the S(4) and S(5) lines were undetected,

we derive T_{32} of $\sim 135\text{--}150$ K, clearly lower than the temperature derived for the sources where the S(4) and S(5) lines were detected. There is no clear dependence of T_{32} on the distance to the Galactic center. However, it is noteworthy that the two clouds with lower T_{32} are located in the Sgr C complex, one of them in the non-thermal filament.

Obviously, T_{32} lacks of physical sense if the ortho-H₂ and para-H₂ abundances are not in equilibrium. As mentioned, we can obtain smooth population diagrams assuming OTP ratios lower than the LTE ratio. The temperature T_{32} derived in this case (T_{32}^{corr}) is higher than the one derived directly from the observations (T_{32}). For instance, assuming OTP ratios ~ 2 one obtains a T_{32}^{corr} which is $\sim 10\%$ larger than T_{32} .

It is possible to estimate the total warm H₂ column densities (N_{H_2}) by extrapolating the populations in the $J=2$ level to the $J=1$ and $J=0$ levels at the temperature T_{32} . The derived warm N_{H_2} are listed in Table 4 and should be considered lower limits to the actual amount of warm molecular gas since the lowest levels can be populated with colder, although still warm, gas. The total column density of warm H₂ varies from source to source but it is typically of $1\text{--}2 \cdot 10^{22}$ cm⁻². These column densities are only a factor of 1.2 higher than those one would obtain without any extinction correction. Thus, in regard to the derived gas temperatures and total column densities, the extinction correction is not critical. On the other hand, extrapolating the column densities in the $J=6$ and $J=7$ to lower levels at the temperature T_{76} , one finds that the amount of gas at ~ 600 K is less than 1% of the column densities measured at ~ 150 K. The H₂ total column densities at temperatures T_{32}^{corr} assuming an OTP ratio of ~ 2 are lower than those of Table 4 by a factor of 1.8. Note, that in this case the total column density should be derived extrapolating the *observed* population in the $J=3$ to the $J=1$ level and the population in the $J=2$ to the $J=0$ levels, as two different species at temperature T_{32}^{corr} . Of course, these column densities are still lower limits to the actual warm H₂ column densities.

These results are the first direct estimation of the H₂ column densities and the structure of the warm gas in the GC clouds. They show the presence of large column densities of warm molecular gas with large temperature gradients (150–700 K), extending the results derived by Hüttemeister et al. (1993) from their NH₃ data.

5. Discussion

5.1. Warm H₂ to CO and NH₃ ratios

As mentioned in Sect. 2.2, we cannot identify which velocity components seen in CO are associated to the warm H₂. Furthermore, the bulk of the CO seen in the $J = 1 \rightarrow 0$ and $J = 2 \rightarrow 1$ lines do not show the characteristics of warm CO associated to the warm H₂ (see Sect. 3). In the following, we will estimate the ratio of the warm H₂ col-

umn densities observed with ISO to the H₂ column densities derived from the CO using LVG calculations. We have added the column densities of each velocity component in every source. These total H₂ column densities are listed in Table 5. One can compare the maximum column densities derived from CO to the H₂ column densities listed in Table 4 to derive a lower limit to the fraction of warm molecular gas with respect to the gas emitting in CO. These ratios are given in Table 5 for all the molecular clouds. We find that the warm H₂ is about $\sim 30\%$ of the H₂ column densities measured from CO. For a few clouds the fraction of warm gas is as high as 77% ($M-0.50 - 0.03$) or even $\sim 100\%$ for $M-0.96 + 0.13$. This implies that, for two clouds all the CO emission should arise from warm gas.

Table 5 also lists the NH₃ abundances in the warm ($X(\text{NH}_3)_{\text{warm}}$) and cold components ($X(\text{NH}_3)_{\text{cold}}$). The $X(\text{NH}_3)_{\text{warm}}$ has been derived from the column densities of warm ammonia (Hüttemeister et al. 1993) and our warm H₂ column densities. We find that, $X(\text{NH}_3)_{\text{warm}}$ is within a range of $3 \cdot 10^{-8}$ to $4 \cdot 10^{-7}$. On the other hand, $X(\text{NH}_3)_{\text{cold}}$ has been derived from the cold ammonia column densities of Hüttemeister et al. and the H₂ column densities derived from the ¹³CO data. In this case, we have taken into account only the ¹³CO velocity components with NH₃ emission and we have assumed that, in average, $\sim 70\%$ of the gas traced by CO is cold gas. With these assumptions, $X(\text{NH}_3)_{\text{cold}}$ varies between $4 \cdot 10^{-8}$ and $6 \cdot 10^{-6}$, being the average value $\sim 5 \cdot 10^{-7}$. This is similar to the abundance in the warm component, and approximately 10 times higher than the “typical” interstellar ammonia abundance (Irvine et al. 1987). The high NH₃ abundances in the cold gas point to the existence of a cold post-shocked gas component as suggested by Hüttemeister et al. (1998) to explain the SiO emission in the GC clouds.

5.2. Heating mechanism

What is the heating mechanism that produces such a large amount of warm molecular gas in the GC? Shocks have been invoked to explain the widespread distribution and the large abundances of refractory molecules like SiO (Martín-Pintado et al. 1997, Hüttemeister et al. 1998), the high temperatures observed in NH₃ (Wilson et al. 1982, Güsten et al. 1985) and the non-equilibrium H₂ ortho-to-para ratio of two sources in our sample (Rodríguez-Fernández et al. 2000). The high NH₃ abundance derived in the previous section points to a mechanical heating mechanism since the ammonia molecule is easily photo-dissociated by ultraviolet radiation. The small column densities of warm dust in these clouds also points to a mechanical heating mechanism (Martín-Pintado et al. 1999).

On the other hand, in some of the clouds we have detected line emission from ionized species like Ne II, Ne III or O III, that should arise in an H II region ionized by ultraviolet (UV) photons (Martín-Pintado et al. 1999, 2000). This

implies that, at least in those clouds, there must be a PDR in the interface between the H II region and the molecular material. Large scale emission of the H₂ $v=1-0$ S(1) line has also been interpreted as arising from PDRs of density $n \sim 10^4$ cm⁻³ and incident far-UV flux of $G_0 \sim 10^3$ (in units of $1.6 \cdot 10^{-3}$ ergs cm⁻² s⁻¹) in the clouds surfaces (Pak, Jaffe & Keller 1996). The total visual extinction of ~ 30 mag derived for the clouds of our sample matches the expected *foreground* extinction and suggest that the pure-rotational H₂ emission could also arise in the surfaces of the clouds as the ro-vibrational lines.

We have compared the population diagrams obtained for the GC clouds with the same type of diagrams predicted by models of C-shocks, J-Shocks and PDRs. Figure 6a shows the comparison between the predictions of a C-Shock from Draine et al. (1983), a J-Shock from Hollenbach & McKee (1989), and the data for M-0.32-0.19. The S(1) to S(5) lines (squares) can be explained with both a C-Shock with velocity of ~ 12 km s⁻¹ acting on gas with preshock density of 10^6 cm⁻³ (circles) or a J-Shock of 50 km s⁻¹ and preshock density of 10^6 cm⁻³ (triangles). However, the observed emission in the S(0) line is ~ 3 times larger than the predicted by both models.

Figure 6b shows the population diagram for M+0.16-0.10 (squares) versus the prototypical reflection nebula NGC 7023 (triangles). As discussed by Fuente et al. (1999), the H₂ emission from this source is well fitted by the PDR model of Burton et al. (1990, 1992) with $G_0 = 10^4$ and $n=10^6$ cm⁻³ although with an OTP ratio of 1.5-2. Comparing the NGC 7023 population diagram with M+0.16-0.10, one finds that the agreement is excellent for the S(4) and S(5) lines but it is not so good for the lowest lines, even taking into account the non-equilibrium OTP ratio found in NGC 7023. In particular, the GC clouds exhibit more emission in the lowest lines than expected from the PDR model for $G_0 = 10^4$ and $n=10^6$ cm⁻³. In contrast, the H₂ $v=1-0$ S(1) intensity predicted by this PDR model is a factor of ~ 10 larger than observed by Pak, Jaffe & Keller (1996). This fact would imply that the vibrational line emission is more diluted in a $3'$ beam than the pure-rotational lines in the SWS beam or that the PDR models do not apply.

In any case, the observed curvature of the population diagrams seems to be in good agreement with the predicted temperature gradient in a PDR. In Fig. 6b, we also show the population diagram one obtains integrating the H₂ emission in LTE with the temperature and H₂ abundance profiles along the $G_0=10^4$ and $n=10^6$ cm⁻³ PDR model of Burton et al. (1990). The result differs from that of Burton et al. in that we do not take into account any radiative pumping, which affects mainly to higher levels than those involved in the S(0) and S(1) lines. Although the GC emission is ~ 3 times larger, it is evident that the shape of the population diagram is very similar to that observed.

With regard to those sources where the S(4) and S(5) were not detected, the upper limits imply that if they are PDR-excited the density must be somewhat lower than $n=10^6$ cm⁻³, or if shock-excited, the shock velocity should be slightly lower than those of the models plotted in Fig. 6.

Both shock and PDR models suggest densities as high as 10^6 cm⁻³ and fail to explain the observed intensity of the S(0) emission and to less extend the S(1) line. The densities implied by the models seem somewhat large, but it looks like the H₂ traces two components: a hot (~ 500 K) and dense ($\lesssim 10^6$ cm⁻³) component necessary to explain the observed S(4) and S(5) lines, and a warm component (~ 150 K) traced by the S(0) and S(1) lines. To match the measured $J = 2 \rightarrow 1/J = 1 \rightarrow 0$ ¹³CO and C¹⁸O ratios the warm H₂ component should have densities of $\sim 10^3$ cm⁻³ (see Sect. 3). The hot and dense gas would have $J = 2 \rightarrow 1/J = 1 \rightarrow 0$ ¹³CO ratios of $\sim 4 - 5$ but it would emit mainly in the high- J CO lines. In any case, the column density of hot and dense gas is very small to make it detectable in the low- J CO lines when mixed with the colder and less dense gas that dominates the emission of these lines.

To explain the derived $T_{32} \sim 150$ K is necessary to invoke PDRs with $G_0 \sim 10^3$ and $n \sim 10^3$ cm⁻³, but to obtain the observed intensities ~ 20 of such PDRs are needed. J-shock models do not predict temperatures as low as 150 K. Moreover, the high velocities required to explain our data are difficult to reconcile with the observations. C-shocks could explain the observed S(0) and S(1) emission with, at least, 10 shocks with velocities as low as ~ 7 km s⁻¹ and $n=10^6$ cm⁻³ (even more shock fronts are needed for lower gas densities). In addition, dissipation of supersonic turbulence could heat the gas to temperatures of ~ 150 K (Wilson et al. 1982; Güsten et al. 1985) and thus, could contribute to the emission in the two lowest H₂ lines. The origin of the turbulence would be the movement of dense clumps in a less dense inter-clump medium due to the differential Galactic rotation and the tidal disruption of the clumps.

The heating rate by dissipation of supersonic turbulence can be estimated as $\Gamma \sim 3.5 \cdot 10^{28} v_t^3 n_{\text{H}_2} (1\text{pc}/l)$ erg s⁻¹ cm⁻³ (Black 1987), where l and v_t are the spatial scale and the velocity of the turbulence, respectively. Taking $v_t \sim 15$ km s⁻¹ (the typical linewidths of GC clouds), $l = 5$ pc, and $n_{\text{H}_2} = 10^3$ cm⁻³, one obtains $\Gamma \sim 5 \cdot 10^{-22}$ erg s⁻¹ cm⁻³. For the conditions of the warm gas, $T \sim 150$ K and $n_{\text{H}_2} \sim 10^3$ cm⁻³, the cooling is expected to be dominated by H₂ and CO. Le Bourlot et al. (1999) has recently estimated the cooling rate by H₂ (Λ_{H_2}) for a wide range of parameters. For the warm gas component of the GC clouds we obtain $\Lambda_{\text{H}_2} \sim 3 \cdot 10^{-22}$ erg s⁻¹ cm⁻³, which is comparable to the CO cooling rate (see e.g. Goldsmith & Langer 1978) Thus, comparing heating and cooling rates, one finds that the dissipation of su-

personic turbulence could account for the heating of the warm component.

In summary, several agents could heat the warm component, while the hot component should trace the densest gas in the GC clouds heated by a PDR or a shock. For instance, if the inhomogeneous structure revealed in the Sgr B2 envelope by interferometric NH₃ observations (Martín-Pintado et al. 1999) is common in the GC, and due to evolved massive stars as they propose, both C-shocks of $\sim 10 \text{ km s}^{-1}$ (shell expansion) and PDRs (stellar radiation) would be present. However, it is not possible to rule out mechanical heating by large scale shocks. In fact, the high fraction of warm H₂ derived for $M-0.96 + 0.13$ and the fact that the CO component with positive velocities apparently does not contribute to the H₂ emission suggests this kind of heating since, at this galactic longitude, shocks are expected at negative velocities due to the intersection of x_1 and x_2 orbits in the context of a barred potential (Binney et al. 1991).

6. Summary and conclusions

We have observed the S(0) to S(5) H₂ pure-rotational lines with the SWS spectrometer on-board ISO toward a sample of 18 molecular clouds of the Galactic center region. The S(3) line is strongly affected by dust extinction due to the 9.7 μm band of the silicates. After correcting the H₂ data for extinction using a self-consistent method, and assuming that the ortho- and para-H₂ populations are in equilibrium one finds that the S(0) and S(1) lines indicate temperatures of $\sim 150 \text{ K}$. Extrapolating to the lowest levels at that temperature, a total H₂ column density of $\sim 1 - 2 \cdot 10^{22} \text{ cm}^{-2}$ is derived. This is the first direct estimate of the column density of warm gas in the GC clouds. In addition, it shows a complex temperature structure of the warm gas.

The temperature derived from the S(5) and S(4) levels is $\sim 600 \text{ K}$ in the sources in which it can be derived, however the column density of gas at this temperature is less than 1% of the column density at $T=150 \text{ K}$. Assuming an OTP ratio of ~ 2 the temperatures would be 10% larger than those derived assuming a LTE OTP ratio, while the total H₂ column densities at those temperatures would be a factor of ~ 1.8 lower than the column densities derived assuming the ortho- and para-H₂ populations in equilibrium. Comparing the H₂ warm column densities with the column densities derived from our CO data by LVG calculations one finds that the average fraction of warm H₂ to the gas observed in CO is $\sim 30\%$. With our data and the NH₃ observations of Hüttemeister et al. (1993) we derive relatively high NH₃ abundances of a few 10^{-7} in both the warm and the cold components.

Several indirect arguments point to shocks as the heating mechanism of the warm gas but PDRs may also play a role. Direct comparison of the H₂ data with PDRs and shocks models indicate that the S(4) and S(5) trace the

densest gas in the GC clouds ($\lesssim 10^6 \text{ cm}^{-3}$) heated in PDRs or shocks. Nevertheless, such dense PDRs or shocks fail to explain the S(0) and S(1) lines: several less dense PDRs, low velocity shocks ($< 10 \text{ km s}^{-1}$) or both along the line of sight would be needed to explain the observed emission.

The cooling by H₂ in the warm component of GC clouds is comparable to the cooling by CO. Equating the H₂ cooling rate with the heating rate by dissipation of supersonic turbulence, one finds that this mechanism could also contribute to the emission in the two lowest H₂ lines. In one source ($M-0.96 + 0.13$), we have also found some evidence of large scale shocks that should be checked with higher spectral resolution H₂ observations.

Acknowledgements. We thank the referee, Rolf Güsten, for his useful comments. We acknowledge support from the ISO Spectrometer Data Center at MPE, funded by DARA under grant 50 QI 9402 3. NJR-F, JM-P, PdV, and AF have been partially supported by the CYCIT and the PNIE under grants PB96-104, 1FD97-1442 and ESP99-1291-E. NJR-F acknowledges *Consejería de Educación y Cultura de la Comunidad de Madrid* for a pre-doctoral fellowship.

References

- Bally J., Stark A.A., Wilson R.W., Henkel C., 1987, ApJS 65, 13
- Binney J., Gerhard O. E., Stark A. A., Bally J., Uchida K. I., 1991, MNRAS 252, 210
- Black J. H., 1987, Interstellar Processes, 731
- Burton M. G., Hollenbach D. J., Tielens A. G. G. M., 1990, ApJ 365, 620
- Burton M. G., Hollenbach D. J., Tielens A. G. G. M., 1992, ApJ 399, 563
- Catchpole R. M., Whitelock P. A., Glass I. S. 1990, MNRAS 247, 479
- Cox P. & Laureijs R., 1989, IRAS Observations of the Galactic Center. in: Morris M. (ed.) Proc. IAU Symp. 136, The Center of the Galaxy. Kluwer, Dordrecht, p. 121
- Dahmen G., Huttemeister S., Wilson T. L., Mauersberger R., et al., 1997, A&AS 126, 197
- Danby G., Flower D. R., Valiron P., Schilke P., Walmsley C. M., 1988, MNRAS 235, 229
- Draine B. T., Roberge W. G., Dalgarno A., 1983, ApJ 264, 485
- Draine B.T., 1989, in: Kaldeich B.H. (ed.) Infrared Spectroscopy in Astronomy, ESA SP-290, 93
- Fuente A., Martín-Pintado J., Rodríguez-Fernández N.J., Rodríguez-Franco A., de Vicente, P., 1999, ApJ 518, L45
- Fuente A., Martín-Pintado J., Rodríguez-Fernández N. J., Cernicharo J., Gerin, M., 2000, A&A 354, 1053
- Goldsmith P. F. & Langer W. D., 1978, ApJ 222, 881
- de Graauw Th., Haser L.N., Beintema D.A, et al., 1996, A&A 315, L49
- Güsten R., Walmsley C. M., Pauls T., 1981, A&A 103, 197
- Güsten R., Walmsley C. M., Ungerechts H., Churchwell E., 1985, A&A 142, 381
- Hollenbach D. & McKee C. F., 1989, ApJ 342, 306
- Hüttemeister S., Wilson T.L., Bania T.M., Martín-Pintado J., 1993, A&A 280, 255

Hüttemeister S., Dahmen G., Mauersberger R., Henkel C., Wilson T.L., Martín-Pintado J., 1998, A&A 334, 646

Irvine W. M., Goldsmith P. F., Hjalmarson A., 1987, *Interstellar Processes*, 561

Kessler M.F., Steinz J.A., Anderegg M.E., et al., 1996, A&A 315, L27

Kunze D., Rigopoulou D., Genzel R., Lutz, D., 1999, *The Universe as Seen by ISO*. Eds. P. Cox & M. F. Kessler. ESA SP-427, 909

Le Boulrot J., Pineau Des Forêts G., Flower, D. R. 1999, MN-RAS 305, 802

Lis D. C. & Carlstrom J. E. 1994, ApJ 424, 189

Lutz D., 1999, in: Cox P. & Kessler M. (eds.) *The Universe as Seen by ISO*, ESA SP-427, 623

Lutz D., Feuchtgruber H., Morfill J., 2000, MPE-ISO-99-1

Martín-Pintado J., de Vicente P., Fuente A., Planesas P., 1997, ApJ 482, L45

Martín-Pintado J., Rodríguez-Fernández N.J., de Vicente P., Fuente A., Wilson T.L., Hüttemeister S., Kunze D., 1999, in: Cox P. & Kessler M. (eds.) *The Universe as Seen by ISO*, ESA-SP 427, 711

Martín-Pintado J., Gaume R.A., Rodríguez-Fernández N.J., de Vicente P., Wilson T.L., 1999b, ApJ 519, 667

Martín-Pintado J., Rodríguez-Fernández N. J., de Vicente P., Fuente A., Wilson T. L., Hüttemeister S., Kunze D., 2000, *ISO beyond the peaks: The 2nd ISO workshop on analytical spectroscopy*, held 2-4 February 2000, at VILSPA., ESA SP-456, in press

Morris M., Polish N., Zuckerman B., Kaifu N., 1983, AJ 88, 1228

Morris M. & Serabyn E., 1996, ARA&A, 34, 645

Odenwald S.F. & Fazio G.G., 1984, ApJ 283, 601

Pak S., Jaffe D. T., Keller L. D., 1996, ApJ 457, L43

Rodríguez-Fernández N.J., Martín-Pintado J., de Vicente P., Fuente A., Hüttemeister S., Wilson T.L., Kunze D., 2000, A&A 356, 695

Rosenthal D., Bertoldi F., Drapatz S., 2000, A&A 356, 705

Salama A., Feuchtgruber H., Heras A., et al., 1997. In: Heras A.M., Leech K., Trams N.R., Perry M. (eds.) *First ISO Workshop on Analytical Spectroscopy*. ESA, Noordwijk, SP-419, p. 17

Shull J.M. & Beckwith S., 1982, ARA&A 20, 163

Timmermann R., Bertoldi F., Wright C. M., Drapatz S., Draine B. T., Haser L., Sternberg A., 1996, A&A 315, L281

Turner J., Kirby-Docken K., Dalgarno A., 1977, ApJS 35, 281

Valentijn E.A., Feuchtgruber H., Kester D.J.M., et al., 1996, A&A 315, L60

van den Ancker, M. E., 1999, Ph.D. Thesis, Amsterdam University

Wilson T.L., Ruf K., Walmsley C.M., Martin R.N., Pauls T.A., Batrla W., 1982, A&A 115, 185

Wilson T.L. & Matteucci F., 1992, A&AR 4, 1

Wright, C.M., 2000, in: Y.C. Minh & E.F. van Dishoeck (eds.) *IAU Symposium 197, Astrochemistry: From Molecular Clouds to Planetary Systems*, Astronomical Society of the Pacific, p177.

Table 1. J2000 coordinates of the sources

Source	RA h m s	DEC ° ' "	Complex
M-0.96 + 0.13	17:42:48.3	-29:41:09.1	Sgr E
M-0.55 - 0.05	17:44:31.3	-29:25:44.6	Sgr C
M-0.50 - 0.03	17:44:32.4	-29:22:41.5	Sgr C
M-0.42 + 0.01	17:44:35.2	-29:17:05.4	Sgr C
M-0.32 - 0.19	17:45:35.8	-29:18:29.9	Sgr C
M-0.15 - 0.07	17:45:32.0	-29:06:02.2	Sgr A
M+0.16 - 0.10	17:46:24.9	-28:51:00.0	Arc
M+0.21 - 0.12	17:46:34.9	-28:49:00.0	Arc
M+0.24 + 0.02	17:46:07.9	-28:43:21.5	Dust Ridge
M+0.35 - 0.06	17:46:40.0	-28:40:00.0	
M+0.48 + 0.03	17:46:39.9	-28:30:29.2	Dust Ridge
M+0.58 - 0.13	17:47:29.9	-28:30:30.0	Sgr B
M+0.76 - 0.05	17:47:36.8	-28:18:31.1	Sgr B
M+0.83 - 0.10	17:47:57.9	-28:16:48.5	Sgr B
M+0.94 - 0.36	17:49:13.2	-28:19:13.0	Sgr D
M+2.99 - 0.06	17:52:47.6	-26:24:25.3	Clump 2

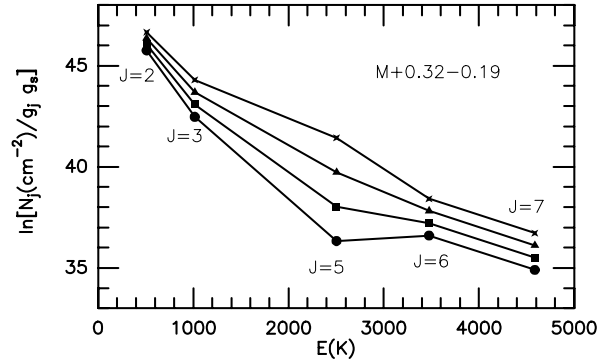
**Fig. 4.** Population diagrams for M-0.32 - 0.19 without any extinction correction (circles) and corrected for 15 (squares), 30 (triangles), and 45 mag. (stars) of visual extinction (A_V). We have assumed the relative extinctions derived toward the Galactic center by Lutz (1999). Note that a smooth curve is obtained with $A_V \sim 30$ mag.

Table 4. Total H₂ column densities and rotational temperatures between the $J=3$ and the $J=2$ levels (T_{32}) and between the $J=7$ and the $J=6$ levels (T_{76}) after correcting for extinction. Numbers in parentheses are 1σ errors of the last significant digits as derived from the fluxes errors in the Gaussian fits of the lines.

Source	A_V	T_{32} K	T_{76} K	$N_{H_2}(T_{32})$ 10^{22} cm^{-2}
M-0.96 + 0.13	15	157(6)	–	1.10(9)
M-0.55 – 0.05	30	135(5)	–	2.7(3)
M-0.50 – 0.03	30	135(4)	–	2.3(2)
M-0.42 + 0.01	30	167(6)	–	1.03(8)
M-0.32 – 0.19	30	188(5)	650(90)	1.03(5)
M-0.15 – 0.07	30	136(6)	–	2.6(4)
M+0.16 – 0.10	30	157(7)	900(200)	1.17(13)
M+0.21 – 0.12	30	186(13)	670(110)	0.64(7)
M+0.24 + 0.02	30	163(2)	–	1.73(6)
M+0.35 – 0.06	30	195(11)	700(200)	0.66(5)
M+0.48 + 0.03	30	174(7)	≤600	1.03(9)
M+0.58 – 0.13	30	149(5)	–	1.3(2)
M+0.76 – 0.05	30	181(4)	–	1.77(8)
M+0.83 – 0.10	30	178(5)	550(60)	1.59(6)
M+0.94 – 0.36	15	146(7)	–	0.95(10)
M+2.99 – 0.06	15	152(3)	–	1.40(9)

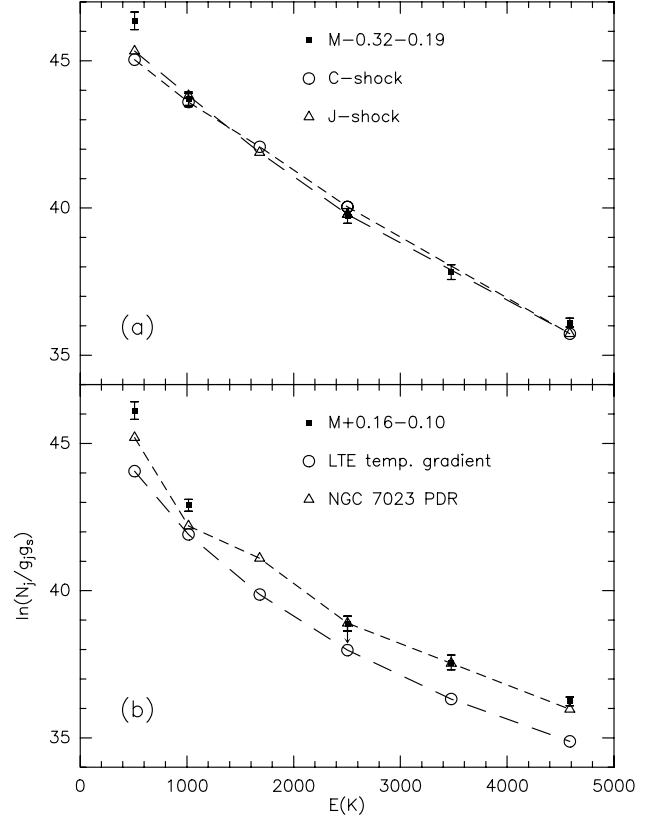


Fig. 6. a: Population diagram for M-0.32 – 0.19 (open squares) corrected for 30 mag. of visual extinction. The errorbars represent upper limits to the flux calibration uncertainties (see text). For comparison, it also displays the population diagrams derived from the model of Draine et al. (1983) of a shock with velocity $\sim 12 \text{ km s}^{-1}$ and preshock density 10^6 cm^{-3} (circles and dashed lines). Triangles and long-dashed lines are used to plot the population diagram derived from the J-shock model of Hollenbach & McKee (1989) for a velocity of 50 km s^{-1} and a preshock density of 10^6 cm^{-3} . **b:** Comparison of the population diagram derived for M+0.16 – 0.10 (open squares) with the results of Fuente et al. (1999) for the NGC 7023 PDR (triangles and dashed line) and the population diagram one obtains integrating the H₂ emission along the temperature and H₂ abundance gradient derived by Burton et al. (1990) for a PDR with density of 10^6 cm^{-3} and $G_0 = 10^4$ (open circles)

Table 2. Observational parameters and LVG results for the CO data: Integrated intensities of the $J = 1 \rightarrow 0$ transitions of C¹⁸O and ¹³CO and C¹⁸O $J = 2 \rightarrow 1$ to $J = 1 \rightarrow 0$ line intensity ratio. Column densities and n_{H_2} derived from the LVG calculations. N_{H_2} derived from $N_{^{13}\text{CO}}$ assuming a ¹³CO abundance relative to H₂ of $5 \cdot 10^{-6}$. Numbers in parentheses are 1σ errors of the last significant digit.

Source	¹³ CO v_{lsr} km s ⁻¹	¹³ CO $I_{(1-0)}$ K km s ⁻¹	C ¹⁸ O $I_{(1-0)}$ K km s ⁻¹	$I_{(2-1)}^{\text{C}^{18}\text{O}}/I_{(1-0)}^{\text{C}^{18}\text{O}}$	$\log(n_{\text{H}_2})^{\text{a}}$ $\log(\text{cm}^{-3})$	$N_{\text{C}^{18}\text{O}}^{\text{a}}$ 10^{15} cm^{-2}	$N_{^{13}\text{CO}}^{\text{a}}$ 10^{16} cm^{-2}	N_{H_2} 10^{21} cm^{-2}
M-0.96 + 0.13	-110	9.9(7)		1.2(3) ^c	3.5-4		0.54-1.1	1.1-2.2
	11	24(1)		0.7(2) ^c	3.2-3.6		0.54-2.1	1.1-4.2
	133	30.2(6)		0.8(1) ^c	3.3-3.5		1.9-2.4	3.8-4.8
M-0.55 - 0.05	-102	126(3)	11.2(5)	2.2(1)	4-4.4	8.9-14.1	14.4-18.2	28.8-36.4
	-60	45(2)	3.2(4)	2.5(4)	>4.2	3.1-5.0	5.4-8.6	10.8-17.2
	-2	23(2)	3.5(4)	1.7(3)	3.8-4	2.7-3.3	1.9-3.0	3.8-6.0
M-0.50 - 0.03	-98	119(5)	20(2)	0.9(1)	3.4-3.7	12-15	12-15	24-30
M-0.42 + 0.01	-87	66(4)	6.6(11)	1.7(4)	4-4.5	4.5-7.1	6.0-9.5	12-19
	-74	54(4)	3.0(8)	2.0(7)	>4	1.9-3.8	4.7-7.5	9.4-15
M-0.32 - 0.19 ^b	-77	16(2)			>3		0.95-2.4	1.9-4.8
	-31	40(2)			>3		2.7-5.4	6.4-10.8
	23	24(2)			>3		1.5-3.4	3.0-6.8
M-0.15 - 0.07	5	120(7)	16.1(4)	1.3(1)	3.7-3.9	1.3-1.6	20-25	40-50
	36	155(7)	13.8(7)	1.2(1)	3.5-4.1	8.3-13.1	13-17	26-34
M+0.16 - 0.10	-8	38(5)	2.8(4)	1.7(3)	3.8-4.2	1.8-2.8	3.2-4.5	6.4-9
	64	97(8)	9.2(5)	2.0(2)	3.9-4.1	6.9-8.7	12.7-16	25.4-32
	81	34(8)	2.7(4)	1.6(4)	>3.7	1.6-3.5	2.5-4.0	5-8
M+0.21 - 0.12 ^b	66	42(3)		0.3(1)	>3		2.9-5.9	5.8-11.8
	100	14(3)		0.2(1)	>3		0.92-1.8	1.8-3.6
M+0.24 + 0.02	30	190(5)	17.7(11)	1.0(1)	3.5-3.9	10-16	16-25	32-50
	66	66(3)	7.0(5)	1.1(2)	3.6-3.8	4.5-5.6	8.2-10.3	16.4-20.6
M+0.35 - 0.06	22	44(2)		1.7(1) ^c	4-4.1		3.8-6.0	7.6-12.0
	75	38.7(13)		1.9(1) ^c	4.4-4.8		3.1-4.9	6.2-9.8
	94	24.2(11)		1.4(1) ^c	3.8-4		1.7-2.5	3.4-5.0
M+0.48 + 0.03	14	58(7)		1.4(2) ^c	3.8-4.2		4.8-6.0	9.6-12.0
	33	107(7)		1.1(1) ^c	3.6-3.8		11-12	22-24
M+0.58 - 0.13	36	143(4)		1.1(1) ^c	3.6-3.7		13-16.7	26-33.4
	87	36(4)		1.3(2) ^c	3.7-3.9		2.4-3.0	4.8-6.0
M+0.76 - 0.05	-40	20(3)	3.4(11)	0.6(4)	2.8-4.2	1.8-4.4	1.3-5.2	2.6-10
	33	281(5)	31(2)	1.6(2)	3.7-4.3	19-37	25-30	50-60
	84	72(3)	8.0(11)	0.9(2)	3.3-3.6	4.1-6.5	6.5-8.2	13-16
M+0.83 - 0.10	-40	9.4(9)	1.8(4)	≤0.8	<3.2	>0.9	≥5.6	≥11.2
	5	46(3)	6.1(7)	0.6(1)	3.0-3.3	3.4-6.8	3.4-5.4	6.8-10.8
	32	93(3)	7.7(7)	1.4(2)	3.6-4.5	4.5-9.2	7.5-12	15-24
	96	88(2)	9.2(5)	1.3(1)	3.6-3.8	5.6-7.1	7.6-9.6	15.2-19.2
M+0.94 - 0.36 ^b	-83	13.8(11)			>3		0.9-1.8	1.8-3.6
	-67	18.1(12)			>3		1.2-2.3	2.4-7.2
	-36	39(2)			>3		2.6-5.2	5.2-10.4
	-10	28.2(14)			>3		1.9-3.7	3.8-7.4
M+2.99 - 0.06	-12	37(4)	2.6(14)	2.1(14)	>3.7	1.5-3.0	2.4-4.7	4.8-9.4
	12	34(4)	3.5(11)	0.7(4)	3.0-4.0	2.4-3.8	2.4-6.0	4.8-12.0

^a Minimum and maximum values derived with the LVG code taking into account the 1σ errors in the line intensities.

^b When the ratio 2-1/1-0 could not be obtained, we have assumed $n_{\text{H}_2} \geq 10^3 \text{ cm}^{-3}$ following Hüttemeister et al. 1998.

^c $I_{(2-1)}^{^{13}\text{CO}}/I_{(1-0)}^{^{13}\text{CO}}$ instead of $I_{(2-1)}^{\text{C}^{18}\text{O}}/I_{(1-0)}^{\text{C}^{18}\text{O}}$

Table 3. Fluxes of the H₂ lines as derived from Gaussian fits in units of 10⁻²⁰ W cm⁻². Upper limits are 3 σ values at the instrumental spectral resolution for point sources. Numbers in parentheses are 1 σ errors of the last significant digit as derived from the Gaussian fits. The radial velocities and the widths of the lines with better signal-to-noise ratio (the S(1) lines) are also shown. The errors in the radial velocities are dominated by the wavelength calibration uncertainties (15-30 km s⁻¹ for the S(1) line). Typical 1 σ error of the line widths derived from the Gaussian fits is less than 5 km s⁻¹.

Line	S(0)	S(1)	S(3)	S(4)	S(5)	$v_{S(1)}$	$\Delta v_{S(1)}$
Aper. (" \times ")	20 \times 27	14 \times 27	14 \times 20	14 \times 20	14 \times 20	km s ⁻¹	km s ⁻¹
$\lambda(\mu\text{m})$	28.2188	17.03483	9.66491	8.02505	6.9095		
M-0.96 + 0.13	7.8(9)	18.4(8)	2.2(5)	–	–	-70	270
M-0.55 - 0.05	9.5(14)	9.7(6)	≤ 0.80	≤ 0.78	≤ 2.0	-80	230
M-0.50 - 0.03	8.2(10)	8.4(4)	≤ 0.64	–	–	-60	230
M-0.42 + 0.01	6.2(6)	13.1(7)	≤ 0.70	–	–	-57	230
M-0.32 - 0.19	7.8(6)	23.0(6)	2.1(2)	3.5(7)	5.7(8)	-59	230
M-0.15 - 0.07	9.4(13)	9.9(12)	≤ 1.1	≤ 1.4	≤ 2.8	-35	220
M+0.16 - 0.10	6.1(9)	10.5(7)	≤ 0.9	2.7(6)	6.5(10)	40	180
M+0.21 - 0.12	4.7(9)	13.3(8)	≤ 1.2	2.8(4) ^a	4.8(11) ^a	16	260
M+0.24 + 0.02	9.8(5)	18.9(4)	≤ 0.92	–	–	-6	170
M+0.35 - 0.06	5.3(8)	17.2(6)	≤ 1.0	2.0(7)	3.5 (8)	27	200
M+0.48 + 0.03	6.7(8)	15.9(8)	1.6(3) ^a	2.4(10) ^a	≤ 3.4	17	170
M+0.58 - 0.13	6.0(6)	8.7(7)	≤ 0.96	≤ 0.97	≤ 2.1	4	210
M+0.76 - 0.05	12.4(9)	32.8(8)	2.0(5)	–	–	-18	180
M+0.83 - 0.10	10.8(9)	27.1(4)	2.2(3)	5.6(10)	6.7(8)	16	170
M+0.94 - 0.36	5.7(9)	10.6(5)	≤ 1.2	≤ 1.1	≤ 2.7	-30	190
M+2.99 - 0.06	9.2(6)	19.4(8)	≤ 0.79	–	–	28	190

^a Detections with low signal-to-noise ratio (~ 2.5)

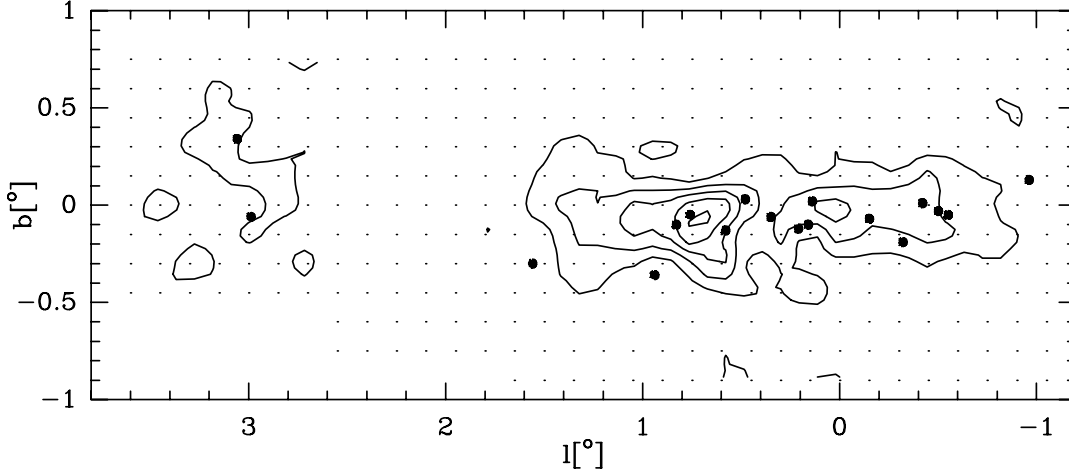


Fig. 1. The positions of all the sources of our sample (including the two clouds presented in Rodríguez-Fernández et al. 2000) overlaid in the C¹⁸O(1-0) map by Dahmen et al. (1997).

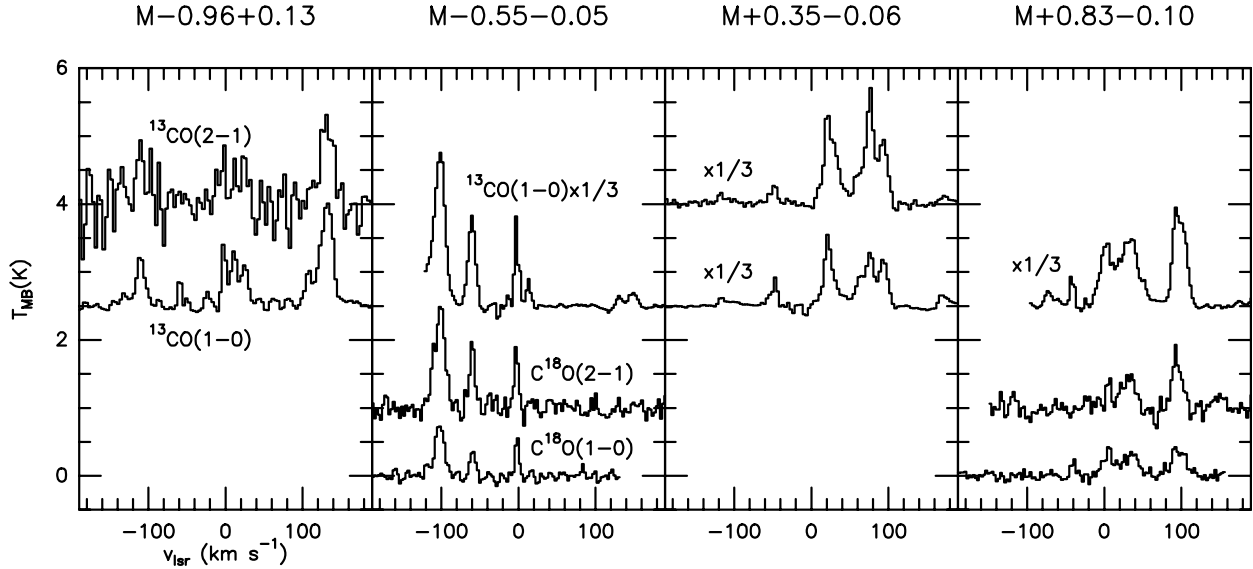
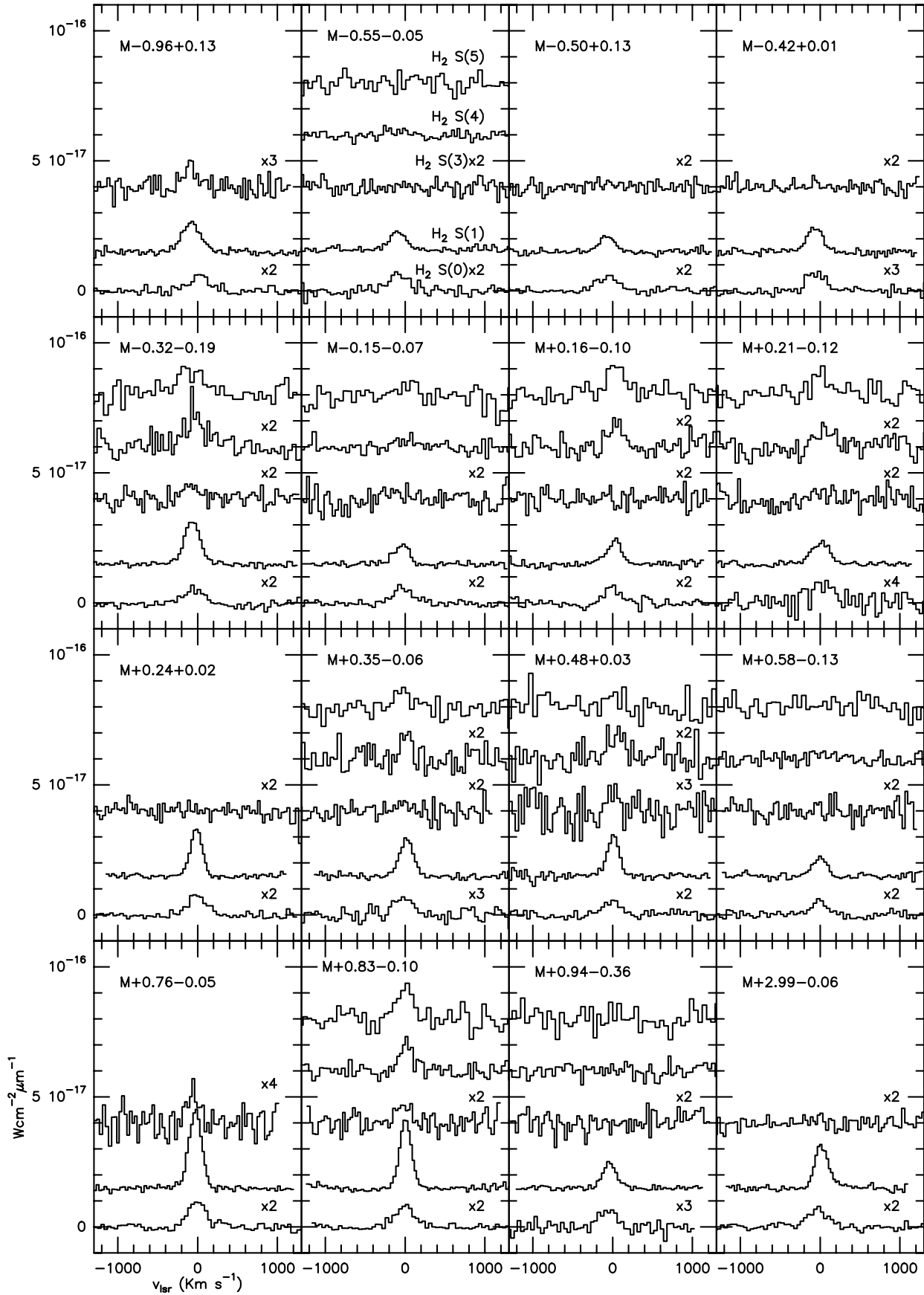


Fig. 2. ¹³CO and C¹⁸O spectra of four sources.

Table 5. Total column densities of H₂ derived from ¹³CO. Fraction of warm N_{H₂} as measured with ISO to the total N_{H₂} derived from ¹³CO. Abundances of NH₃ in the warm and cold components (see text).

Source	$N_{\text{H}_2}^{\text{CO}}$ 10^{22} cm^{-2}	$N_{\text{H}_2}^{\text{warm}}/N_{\text{H}_2}^{\text{CO}}$	$X(\text{NH}_3)_{\text{warm}}$	$X(\text{NH}_3)_{\text{cold}}$
M-0.96 + 0.13	0.6-1.1	1	$3.7 \cdot 10^{-7}$	$4.9 \cdot 10^{-6}$
M-0.55 - 0.05	4.3-6.0	0.45		
M-0.50 - 0.03	2.4-3.0	0.77	$2.6 \cdot 10^{-8}$	$1.6 \cdot 10^{-7}$
M-0.42 + 0.01	2.1-3.4	0.29	$8.3 \cdot 10^{-8}$	$2.9 \cdot 10^{-8}$
M-0.32 - 0.19	1.1-2.2	0.45	$1.8 \cdot 10^{-8}$	$3.1 \cdot 10^{-7}$
M-0.15 - 0.07	6.6-8.4	0.31	$2.4 \cdot 10^{-7}$	$2.7 \cdot 10^{-7}$
M+0.16 - 0.10	3.7-4.9	0.24		
M+0.21 - 0.12	0.8-1.5	0.41		
M+0.24 + 0.02	4.8-7.1	0.24	$1.3 \cdot 10^{-7}$	$8.9 \cdot 10^{-7}$
M+0.35 - 0.06	1.7-2.7	0.25		
M+0.48 + 0.03	3.2-3.6	0.28		
M+0.58 - 0.13	3.1-3.9	0.33		
M+0.76 - 0.05	6.6-8.6	0.21		
M+0.83 - 0.10	4.8-6.5	0.25		$3.4 \cdot 10^{-8}$
M+0.94 - 0.36	1.3-2.9	0.33		$6.7 \cdot 10^{-7}$
M+2.99 - 0.06	1.0-2.1	0.65		$9.0 \cdot 10^{-7}$



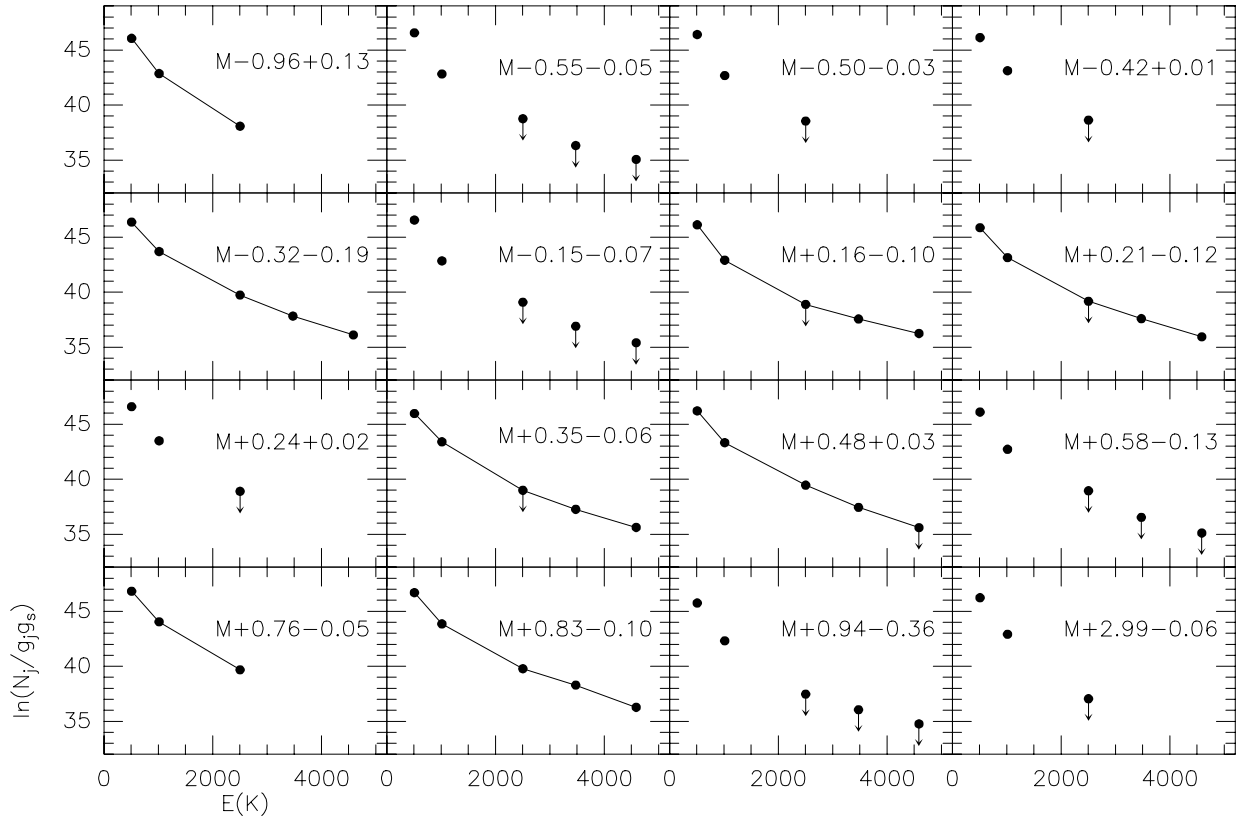


Fig. 5. Population diagrams for all the sources corrected for the extinctions listed in Table 4. The filled circles are connected when more than three lines are detected. Arrows indicate upper limits. The error-bars are smaller than the circles (even taking into account both calibration and Gaussian fitting errors).